

# Network method for voxel-pair-level brain connectivity analysis under spatial-contiguity constraints

Tong Lu<sup>1</sup>, Yuan Zhang<sup>2</sup>, Peter Kochunov<sup>3</sup>, Elliot Hong<sup>3</sup>, Shuo Chen<sup>3,4</sup>

<sup>1</sup>Department of Mathematics, University of Maryland

<sup>2</sup>Department of Statistics, The Ohio State University

<sup>3</sup>Maryland Psychiatric Research Center, School of Medicine, University of Maryland,

<sup>4</sup>Division of Biostatistics and Bioinformatics, School of Medicine, University of Maryland, \*[shuochen@som.umaryland](mailto:shuochen@som.umaryland.edu)

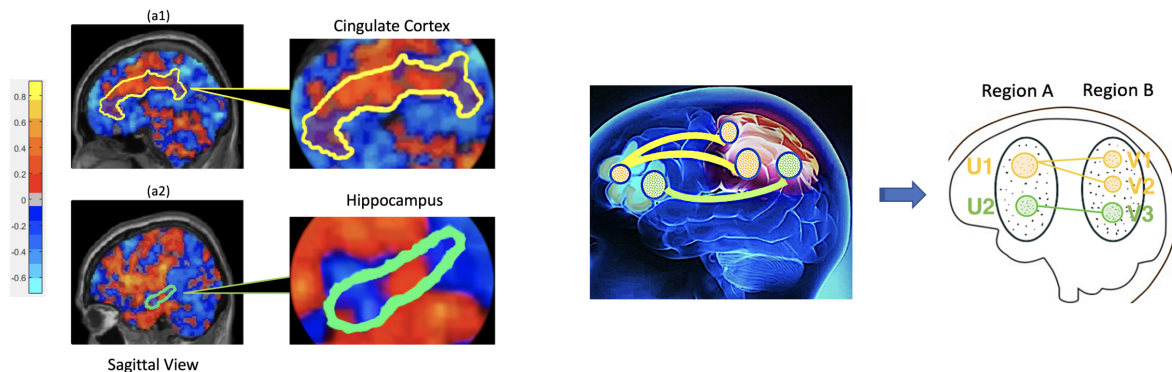
## Abstract

Brain connectome analysis commonly compresses high-resolution brain scans (typically composed of millions of voxels) down to only hundreds of *regions of interest* (ROIs) by averaging within-ROI signals. This huge dimension reduction improves computational speed and the morphological properties of anatomical structures; however, it also comes at the cost of substantial losses in spatial specificity and sensitivity, especially when the signals exhibit high within-ROI heterogeneity. Oftentimes, abnormally expressed *functional connectivity* (FC) between a pair of ROIs caused by a brain disease is primarily driven by only small subsets of voxel pairs within the ROI pair. This article proposes a new network method for detection of voxel-pair-level neural dysconnectivity with spatial constraints. Specifically, focusing on an ROI pair, our model aims to extract dense sub-areas that contain aberrant voxel-pair connections while ensuring that the involved voxels are spatially contiguous. In addition, we develop sub-community-detection algorithms to realize the model, and the consistency of these algorithms is justified. Comprehensive simulation studies demonstrate our method’s effectiveness for reducing the false-positive rate while increasing statistical power, detection replicability, and spatial specificity. We apply our approach to reveal: (i) voxel-wise schizophrenia-altered FC patterns within the salience and temporal-thalamic network from 330 participants in a schizophrenia study; (ii) disrupted voxel-wise FC patterns related to nicotine addiction between the basal ganglia, hippocampus, and insular gyrus from 3269 participants using UK Biobank data. The detected results align with previous medical findings but include improved localized information.

**Keywords:** Keywords: Brain connectome, spatial contiguity, voxel-pair-level connectivity, fMRI

# 1 Introduction

Statistical network analysis and graph theory have been fundamental in the study of the intricate neural circuits in human brains (the “human connectome”) (Bullmore and Sporns, 2009; Rubinov and Sporns, 2010). A large body of literature has revealed that the human connectome is a well-organized obscure network, and it exhibits graph properties of intelligent networks such as social networks and the Internet (Bahrami et al., 2019; Cao et al., 2014). Built on graph theory, brain network analysis depicts the brain connectome as a graph in which cortical regions are denoted as nodes and the connections between regions are edges. Under this framework, abundant statistical models have been developed to study the associations between complex neural connections and experimental/clinical conditions (e.g., Simpson et al. (2013); Fornito et al. (2016)). These models can help to enhance our understanding of the underlying pathophysiological mechanisms of brain diseases (e.g., Alzheimer’s disease and Parkinson’s disease) and assist clinical predictions concerning disease diagnosis and treatment selection.



(a) A demonstration of voxel-level variability within ROIs

(b) An example of covariate-related sub-area connections

Figure 1: (a) shows the heterogeneity of functional connectivity(FC) among intra-ROI voxels from a seed-to-voxel analysis. Here, the insula was used as a seed ROI. The heatmaps in (a) characterize the FC between the seed ROI and voxels in the cingulate cortex (a1) or hippocampus (a2). Both cingulate and hippocampus are well-known ROIs, but their interior FC to insular varies substantially. (b) shows a simplified example of covariate-related FC between voxels in sub-area pairs  $(U_1, V_1)$ ,  $(U_1, V_2)$ , and  $(U_2, V_3)$  from a larger ROI pair (Region A, Region B).

In brain network studies, regions of interest (ROIs) are often considered as basic units of analysis, and these are equivalent to nodes/vertices in graph theory. The popularity of region-level brain network (RBN) analysis comes from its high anatomical consistency and computational tractability. When a whole-brain connectome is considered, RBN analysis dramatically reduces the search dimensions from trillions ( $10^6 \times 10^6$ ) to thousands ( $10^2 \times 10^2$ ). However, RBN analysis relies on the assumption of signal homogeneity among

intra-ROI voxels, which is often violated in reality. When significant intra-ROI heterogeneity is present, RBN analysis can lead to several analytical flaws: *Variability negligence*. Simply averaging the time series of voxels within an ROI can lead to voxel-level information variability loss (e.g., [Figure 1\(a\)](#)); *Spatial specificity loss*. A clinical covariate may alter the ROI-pair connections by disrupting only a small proportion of intra-ROI voxel pairs. In such cases, RBN analysis fails to precisely distinguish the localized alterations; *Power loss*. The averaging process mixes both significant and non-significant voxel-level connections, which often attenuates the effect size and statistical power.

Recently, many brain network studies have shifted focus from RBN analysis to voxel-level network analysis ([Loewe et al., 2014](#); [Wu et al., 2013](#)). Traditional multiple testing methods (e.g., the false-discovery rate (FDR) and the family-wise error rate (FWER) control) are not applicable to high-dimensional multivariate voxel pairs since they are unable to take into account anatomical restrictions and inherent systematical patterns of disease-associated voxels in ROIs. Some other existing methods may also have limitations, such as not utilizing rich voxel-level information to complement region-level connectivity characterization, or yielding relatively hard-to-interpret results for various reasons (e.g., under-represented neurobiological structures or biases in the seed-selection process). Several advanced statistical methods have been proposed to address these limitations. For example, ([Xia and Li, 2017](#)) and ([Xia and Li, 2019](#)) provided localized statistical inference by accounting for the network properties. ([Chen et al., 2016](#)) proposed a Bayesian hierarchical model to identify the voxel-level connectivity patterns associated with clinical covariates and then used the voxel-wise functional connectivity (vFC) patterns to infer region-level connections. These novel approaches yield improved inference results and localized specificity. Nonetheless, they are not directly applicable to our input data of interest (i.e., an  $m \times n$  “bi-cluster” rather than an  $n \times n$  adjacency matrix), and they do not regulate involved voxels to be spatially contiguous. Unlike RBN analysis, spatial contiguity is crucial for vFC analysis because: (i) it preserves anatomical homogeneity, and it hence preserves the interpretability of the vFC results ([Thirion et al., 2006](#)); (ii) it better controls the FDR and FWER since phenotype-related vFC is often intrinsically linked with the topological structure of the brain connectome ([Fan et al., 2012](#)).

In this study, our goal was to identify altered vFC patterns between spatially contiguous sub-area pairs from a larger region pair. More specifically, given a region pair of interest, we sought to extract interior sub-area pairs that could maximally cover spatially adjacent covariate-related vFC with well-controlled FDR and FWER values (e.g., [Figure 1\(b\)](#)). Our sub-area *extraction* approach is fundamentally distinct from other commonly used brain *parcellation* methods such as anatomy-based and data-driven approaches (e.g., gradient- or similarity-based mappings) ([Wig et al., 2014](#); [Craddock et al., 2012](#)); these parcellation methods seek to segment an ROI into different sub-regions, and every single voxel is assigned to a corresponding sub-region. In contrast to parcellation methods in which every voxel is processed, our sub-area extraction approach only selects subsets of voxels that are covariate-related and are constrained in spatially contiguous spaces. All other non-selected voxels are considered to be covariate-indifferent. Sub-area extraction is more suited to our study because: (i) it is likely that the covariate-related differences across

clinical groups may gather in the vFC between a sub-area in Region A and an intersection of multiple sub-areas grouped by the existing parcellation methods in Region B; (ii) it is often found that only a small proportion of voxels in regions A and B are disrupted, and thus a comprehensive parcellation across the entire ROI is not necessary (Cao et al., 2014).

To achieve the desired sub-area extraction and address the limitations discussed above, we propose a new statistical network framework to extract **Spatially Constrained and Connected Networks**, hereafter referred to as SCCN. SCCN is a two-step method (Figure 2) focusing between a pair of ROIs, say A and B, that are believed to contain aberrant functional connections caused by a brain disease. In **step 1**, SCCN extracts spatially coherent sub-area pairs that maximally contain disease-altered vFC between regions A and B. In **step 2**, we formally test each extracted sub-area pair to determine whether it is significantly covariate-associated with multiple testing controls. If no sub-area pairs are found to be significant, we then consider the region-pair connectivity as covariate-unrelated. If significant results are seen, the association between the covariate of interest and the ROI-pair connections can be traced down to smaller but much more precise sub-areas consisting of extracted voxels. These vFC results may provide insights into understanding the latent neurophysiological mechanisms of diseases.

Herein, we show that SCCN provides a consistent estimate for the true community structure in the sense that the error of edge assignments is negligible in large region pairs. We also empirically evaluate the performance of SCCN using two real data examples and considerable simulation studies. In particular, the two real examples use functional magnetic resonance imaging (fMRI) data from a schizophrenia research study with 330 participants and a nicotine-addiction research study using UK Biobank<sup>1</sup> data with 3269 participants. For the schizophrenia data, we focus on the salience network and the temporal-thalamic network, both of which are well known to be susceptible to schizophrenic disorder. SCCN yields spatially coherent sub-area pairs in which most of the interior vFC is disrupted in schizophrenia, notably the (dorsal insula, anterior cingulate cortex) pair and the (anterior/medial temporal gyrus, medial thalamus) pair. For the UK Biobank data, we focus on the basal ganglia, hippocampus, and insular gyrus, which are believed to be vulnerable to the effects of nicotine. Here, SCCN yields spatially coherent sub-areas pairs containing addiction-associated vFC, notably the (medial inferior basal ganglia, medial inferior insula) pair. In contrast, traditional multiple testing correction methods (e.g., FDR and FWER control) and several existing RBN analyses have failed to reveal these findings with voxel-wise topological structures. Moreover, the results of our simulation studies also show that SCCN achieves satisfactory performance in increasing statistical power and spatial specificity while controlling the false-positive rate. In addition, SCCN is easily scalable to both small and large datasets.

---

<sup>1</sup>UK Biobank is a large-scale biomedical database and research resource containing in-depth genetic and health information from half a million UK participants.

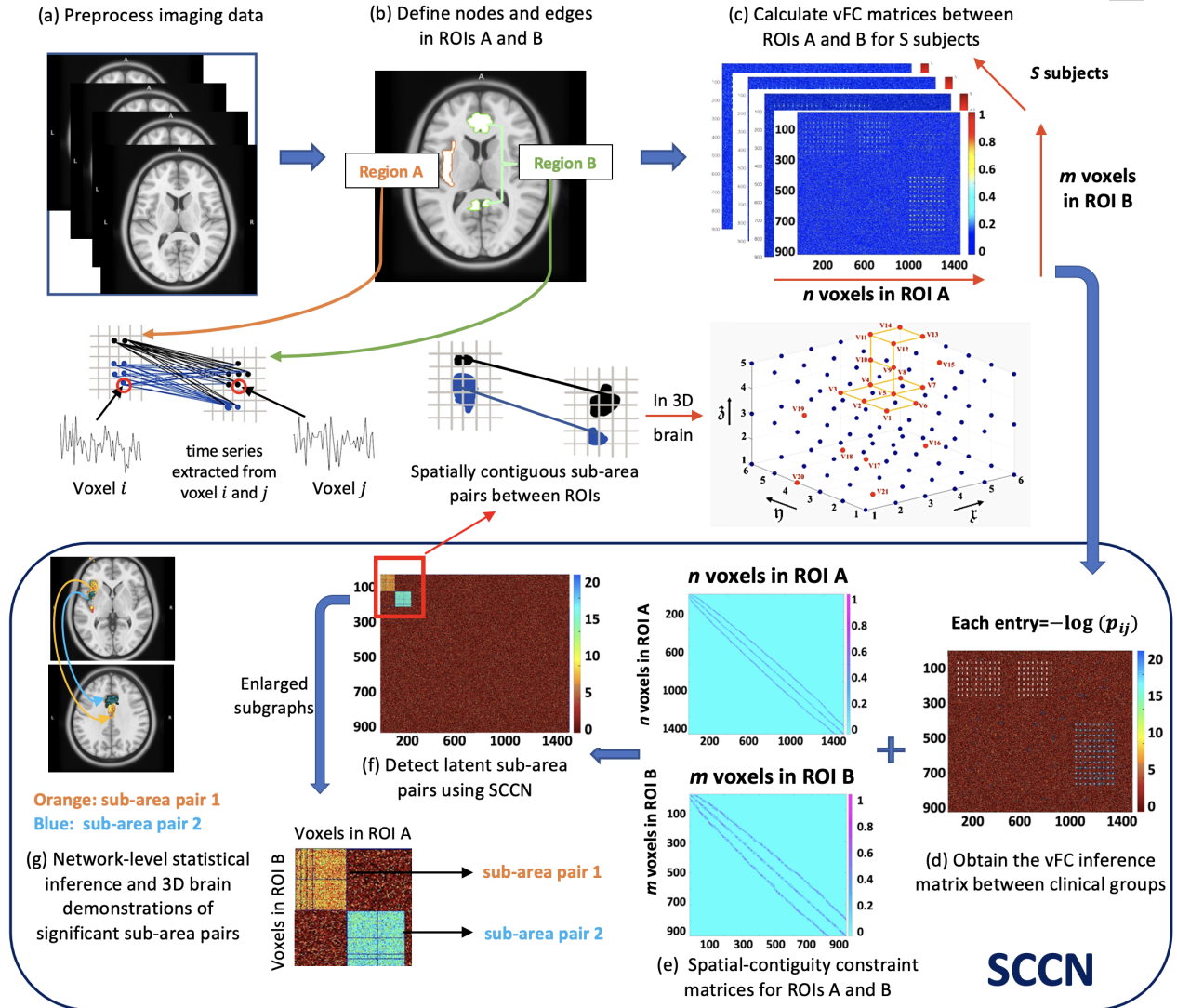


Figure 2: The vFC pattern extraction and inference pipeline. (a) Preprocess the fMRI data to remove unwanted artifacts and transform the data into a standard brain template. (b) Define voxels in ROIs as nodes and bonds between voxels as edges. Extract the time series of brain signals from each voxel. (c) Calculate the connectivity matrix between voxels from two regions, A and B, for each subject. (d) Calculate the connectivity inference matrix, where each element is a test statistic per edge between clinical groups. A hotter point in the heatmap suggests a larger between-group difference. (e) Calculate the spatial-contiguity constraint matrices for ROIs A and B (see detailed matrix construction in Section 2.1). In (e1), each dot represents a voxel in 3D coordinates, where red dots are voxels of interest. Voxels connected by yellow lines form a spatially contiguous area. (f) Detect the disease-related connections contained in sub-area pairs based on (d) and (e) jointly. (f) is obtained by re-ordering the nodes in (d), where the densely altered sub-networks are pushed to the top (i.e., (d) and (f) are isomorphic graphs). (g) Conduct the MDL-based network-level statistical inference. The sub-area pairs that pass the statistical tests are highlighted.

## 2 Methods

### 2.1 Background

#### 2.1.1 Data structure

Focusing on fMRI data, we want to investigate altered vFC patterns between two ROIs, A and B, consisting of  $n$  and  $m$  voxels, respectively. For a subject  $s \in [S] := \{1, \dots, S\}$ , let  $\mathbf{Z}_{n \times T}^{A,s}$  and  $\mathbf{Z}_{m \times T}^{B,s}$  represent the matrices of voxel-level blood-oxygenation-level dependent (BOLD) signals at  $T$  different time points for ROIs A and B. The outcome variables are the functional connectivity measures quantified by similarity matrices between the time series of voxels in A and in B. For example,  $Y_{ij}^s$ , the connectivity strength between voxel  $i$  in A and voxel  $j$  in B, can be computed by  $Y_{ij}^s = f(Z_{i,\cdot}^{A,s}, Z_{j,\cdot}^{B,s})$ , where  $Z_{i,\cdot}^{A,s}$  and  $Z_{j,\cdot}^{B,s}$  are the BOLD time series for voxels  $i$  and  $j$ , and  $f$  is a similarity metric (e.g., Fisher’s  $z$ -transformed Pearson correlation). Collecting all  $Y_{ij}^s$  for each voxel pair  $(i, j) \in [n] \times [m]$  gives an inter-region connectivity matrix  $\mathbf{Y}_{n \times m}^s$ . Additionally, a covariate vector  $\mathbf{X}_{1 \times p}^s$  is observed for each subject  $s$ , and this contains demographic and clinical information.

Our goal is to identify clinical/behavioral-related functional connectivity (FC) patterns at the voxel level. This is because voxel-level findings can reveal altered FC with improved statistical power and enhanced spatial specificity and resolution. To achieve this, multivariate statistical inference is required for the  $n \times m$  vFC outcomes (usually in high dimension, e.g., millions) with spatial constraints. We first test the associations between each outcome  $Y_{ij}^s$  and a regressor of primary interest  $x_1^s \in \mathbf{X}^s$  (clinical status in our application, e.g., patient or control):

$$\mathbb{E}(Y_{ij}^s | \mathbf{X}^s) = \alpha_0 + x_1^s \beta_{ij} + \mathbf{X}_{1 \times (p-1)}^s \boldsymbol{\alpha},$$

where  $\beta_{ij}$  is the coefficient of  $x_1^s$  and  $\boldsymbol{\alpha}$  is a coefficient vector for the remaining covariates  $\mathbf{X}_{1 \times (p-1)}^s$  (e.g., age, ethnicity, etc). We denote  $\boldsymbol{\beta} := \{\beta_{ij}\}_{i \in [n], j \in [m]}$  and aim to systematically extract vFC whose  $\boldsymbol{\beta} \neq 0$  with high accuracy. We further summarize the significance levels of  $\boldsymbol{\beta}$  by a *connectivity inference matrix*  $\mathbf{W}_{n \times m}$ . Each entry of  $\mathbf{W}_{n \times m}$  is computed by  $\mathbf{W}_{ij} = -\log p_{ij}$ , where  $p_{ij}$  is the  $p$ -value for  $\beta_{ij}$ . In neuroimaging statistics, the selection of  $\boldsymbol{\beta} \neq 0$  is not only determined by the level of statistical significance but also by spatial constraints. In addition to these two factors,  $\boldsymbol{\beta}$  is also intrinsically linked with an underlying  $n \times m$  bipartite graph between ROIs A and B. Therefore, we will require both graphic and spatial information to assist in identifying vFC whose  $\boldsymbol{\beta} \neq 0$ . We present the detailed graphic and spatial constructions as follows.

#### 2.1.2 Graph representation

To decipher the complex voxel-pair connectome, we consider a bipartite graph structure  $G = \{U, V\}$  underlying the inference matrix  $\mathbf{W}_{n \times m}$ . The node sets  $U$  and  $V$  represent voxels in ROIs A and B, respectively, where  $|U| = n$  and  $|V| = m$ . We assume that, after spatial normalization and registration of the fMRI data, all subjects share common node sets, namely,  $(U^s, V^s) \equiv (U, V), \forall s \in [S]$ .

### 2.1.3 Spatial contiguity

Each node in our dataset corresponds to a voxel at a certain spatial position in 3D brain imaging (e.g., Figure 2(e1)). When we map each detected subgroup of voxels back to the 3D brain space, we desire these voxels to emerge as a spatially adjacent cluster (i.e., connected components). Such anticipation, translated into formal language, is referred to as *spatial contiguity*. Specifically, we define an “infrastructure graph”  $\mathcal{S}_A$  between all nodes within ROI A to accommodate spatial contiguity. Each entry  $S_{ii'}$  in  $\mathcal{S}_A$  is a spatial-adjacency indicator variable between voxels  $i$  and  $i'$  in ROI A, where  $S_{ii'} = 1$  if  $d_{ii'} \leq \epsilon$ , and  $S_{ii'} = 0$  otherwise ( $d_{ii'}$  is the Euclidean distance between voxels  $i$  and  $i'$ ). For example, in a 3D grid space, when  $\epsilon$  is set to be  $\sqrt{3}$ , a centroid voxel  $i$  in a cube will have 26 surrounding voxels  $i'$  such that  $S_{ii'} = 1$ . We define and interpret  $\mathcal{S}_B$  for nodes within ROI B similarly.  $\mathcal{S}_A$  and  $\mathcal{S}_B$  will be used to prescribe the spatial-contiguity constraints when implementing SCCN. We provide more rigorous mathematical definitions of spatial contiguity,  $\mathcal{S}_A$ , and  $\mathcal{S}_B$  in Appendix A.1.

We propose the SCCN model to systematically select vFC of  $\beta_{ij} \neq 0$  by jointly considering the information of voxel-pair-level statistical significance, underlying graph structures, and spatial constraints. We integrate these into a weighted graph  $\mathcal{G} = \{W, \mathcal{S}_A, \mathcal{S}_B\}$  as the input of our method.

## 2.2 Detecting densely altered sub-area pairs from an ROI pair

### 2.2.1 Spatial-contiguity-constrained objective function

The node set  $U$  corresponding to voxels in ROI A can reportedly be partitioned into mutually non-overlapping sub-areas  $\{U_c\}$ , denoted by  $U = \bigoplus_{c=1}^C U_c$  (Eickhoff et al., 2015). Similarly, we have  $V = \bigoplus_{d=1}^D V_d$  for ROI B. In this paper, we aim to extract sub-area pairs  $\{(U_c, V_d)\}$  that dominantly contain disease-related voxel pairs, and we call these “densely altered” sub-area pairs. Formally, a sub-area pair  $(U_c, V_d)$  is considered densely altered if  $\sum_{(i,j) \in (U_c, V_d)} \frac{I(\beta_{ij} \neq 0)}{|U_c| |V_d|} \gg \sum_{(i,j) \in (U_c', V_d')} \frac{I(\beta_{ij} \neq 0)}{|U_c'| |V_d'|}$ , where  $U_c'$  and  $V_d'$  are the complements of node sets  $U_c$  and  $V_d$ . We are therefore inspired to devise a regularized objective function to generate a checkerboard-like network structure underlying the connectivity inference matrix  $\mathbf{W}$ . This network structure reshuffles  $\mathbf{W}$  and reveals densely altered  $\{(U_c, V_d)\}$  pairs from  $(U, V)$ . In addition, we impose spatial contiguity on  $U_c$  and  $V_d$  to improve biological interpretability and prohibit isolated false positive edges. Finally, the objective function is formulated as follows:

$$\underset{\substack{C, D, U = \bigoplus_{c=1}^C U_c, V = \bigoplus_{d=1}^D V_d \\ (U_c, V_d \text{ subject to spatial contiguity})}}{\operatorname{argmax}} \int \sum_{c=1}^C \sum_{d=1}^D \left\{ \log \frac{\sum_{i \in U_c, j \in V_d} W_{ij} \cdot I(W_{ij} > r)}{|U_c| |V_d|} \right. \quad (1) \\ \left. + \lambda \log(|U_c| |V_d|) \right\} g(r) dr,$$

where  $\lambda \in [0, 1]$  is a tuning parameter,  $r$  is a threshold below which there is no disease-related effect on  $W_{ij}$ , and  $g(r)$  is the distribution function for  $r$ . Both  $g(r)$  and  $\lambda$  can be chosen by prior knowledge or by a data-driven method proposed in Section 2.2.2.

The tuning parameter  $\lambda$  falls in the range  $[0, 1]$ : when  $\lambda = 0$ , maximizing (1) is equivalent to maximizing  $f_1 = \frac{\sum_{i \in U_c, j \in V_d} W_{ij} \cdot I(W_{ij} > r)}{|U_c| |V_d|}$ , which is a popular definition for connection density; when  $\lambda = 1$ , maximizing (1) is simply maximizing  $f_2 = \sum_{i \in U_c, j \in V_d} W_{ij} \cdot I(W_{ij} > r)$ , which quantifies the magnitude of significant voxel pairs contained by the sub-area pair  $(U_c, V_d)$ . Direct optimization of the connection density  $f_1$  tends to detect a dense subgraph with a minuscule size, while the optimization of  $f_2$  can trigger an oversized subgraph. Theorem 1 shows that function (1) provides a consistent estimate for the targeted topological structure (collections of edge-induced sub-area pairs) in the sense that the error of edge assignments is negligible in large region pairs. Extensive simulation studies also show that function (1) performs well in balancing the size and density when detecting subgraphs.

### 2.2.2 Optimization of objective function (1) for given $g(r)$ and $\lambda$

In this section, we focus on optimizing function (1) for a given configuration of  $g(r)$  and  $\lambda$ , which are the density function for the threshold  $r$  and the tuning parameter in (1). We will then discuss how to determine  $g(r)$  and  $\lambda$  in the next section. Unfortunately, even with a given  $g(r)$  and  $\lambda$ , direct optimization of (1) is still an NP-hard problem. Therefore, traditional optimization methods, such as gradient descent, cannot be used due to the non-convexity of the problem. Here, we present an alternative strategy for approaching (1). The essential idea is that we integrate  $\mathbf{W}$  with the spatial-contiguity constraints and then estimate the targeted community structure using modified spectral clustering algorithms via iterative procedures. As presented earlier, the targeted network structure is  $\{U_c, V_d\}$  partitioned from  $(U, V)$  (i.e., the collection of edge-induced sub-area pairs, or in other words, the voxel memberships of  $U_c$  and  $V_d$ ), where  $U = \bigoplus_{c=1}^C U_c$  and  $V = \bigoplus_{d=1}^D V_d$ .

According to the spectral clustering algorithm, applying singular value decomposition to the Laplacian matrix of  $\mathbf{W} = \mathbf{U}\mathbf{\Sigma}\mathbf{V}^\top$  and then clustering  $\mathbf{U}$  and  $\mathbf{V}$  will give partitions of regions A and B, respectively. Now, since  $\mathbf{V}$  is the eigenvectors of  $\mathbf{W}^\top \mathbf{W}$ , spectral clustering on the Laplacian matrix of  $\mathbf{W}^\top \mathbf{W}$  will simply give the partitions of Region B. Similarly, spectral clustering on the Laplacian matrix of  $\mathbf{W}\mathbf{W}^\top$  will provide the partitions of Region A. Therefore, our community-detection algorithm can be conducted based on  $\mathbf{W}\mathbf{W}^\top$  and  $\mathbf{W}^\top \mathbf{W}$ . Next, to incorporate the spatial-contiguity constraints into the optimization, we make use of the two within-region ‘‘infrastructure graphs’’  $\mathcal{S}_A$  and  $\mathcal{S}_B$  introduced earlier. Specifically, we define

$$\mathbf{W}_A = \mathbf{W}\mathbf{W}^\top \odot \mathcal{S}_A \quad \text{and} \quad \mathbf{W}_B = \mathbf{W}^\top \mathbf{W} \odot \mathcal{S}_B, \quad (2)$$

where  $\odot$  is an element-wise product. As pointed out by Kamvar et al. (2003) and Craddock et al. (2012),  $\mathcal{S}_A$  and  $\mathcal{S}_B$  force the similarity between all pairs of non-adjacent voxels to zero, which breaks edges between isolated voxels in the graph. Based on this, the  $n$  by  $n$  matrix  $\mathbf{W}_A(ii')$  (where  $i$  and  $i'$  are two voxels in A) is greater if the voxels in A are spatially adjacent and have a similar profile linking to voxels in Region B. The spatial-contiguity



constraints enable our method to produce results that better honor the neurobiological background regarding the coherence of neighboring neuron populations (Thirion et al., 2006).

We can now fit a stochastic block model to  $\mathbf{W}_A$  (and another to  $\mathbf{W}_B$ ) using the spectral clustering algorithm and then grid search for the optimizer of function (1). We further examine whether the estimated  $\hat{U}_c$  and  $\hat{V}_d$  values satisfy the spatial-contiguity constraints, while empirically we find that the constraints are typically satisfied. There is thus no need to perform any further modification step for the constraints. We formally present our clustering procedure in Algorithm 1.

---

**Algorithm 1** Optimization of objective function (1) with given  $\lambda$

---

```

1: procedure ALGORITHM (Input:  $\lambda$  and  $\mathcal{G} = \{\mathbf{W}, \mathcal{S}_A, \mathcal{S}_B\}$ )
2:   function SCCN.partition ( $\lambda, \mathcal{G}$ )
3:     for  $C = 1, 2, \dots, |U|$  do
4:       Ratio-cut spectral clustering  $\mathbf{W}_A$  into  $C$  networks:  $U = \bigoplus_{c=1}^C U_c$ 
5:       for  $D = 1, 2, \dots, |V|$  do
6:         Ratio-cut spectral clustering  $\mathbf{W}_B$  into  $D$  networks:  $V = \bigoplus_{d=1}^D V_d$ 
7:         Substitute network sets  $U$  and  $V$  into objective function (1), and obtain the output values
8:       end for
9:     end for
10:    return  $C, D, U = \bigoplus_{c=1}^C U_c$  and  $V = \bigoplus_{d=1}^D V_d$  that yield the maximum output value
11:  end function
12: end procedure

```

---

**Consistency for subgraph detection.** In Lemma 1, we first establish that, given true sub-areas numbers  $C^*$  and  $D^*$ , the solution to optimize the objective function (1) provides a consistent estimate for the topological structure of the target community ( $\{U_c, V_d\}$ ) (the collection of edge-induced sub-area pairs) in the sense that false-positive edge assignments are negligible in very large bipartite graphs  $G = (U, V)$ ,  $|U| \rightarrow \infty$ , and  $|V| \rightarrow \infty$ . Then, we establish the convergence of Algorithm 1 to optimize function (1) based on Theorems 1 and 2. In Theorem 1, we prove that our algorithm can provide a consistent estimate of the number of sub-areas, C and D. In Theorem 2, we prove that the implementation of Algorithm 1 converges to the optimal solution of the objective function (1).

To present the theoretical results, we consider the following settings. Let  $\{e_{ij}^1\}$  and  $\{e_{ij}^0\}$  be the sets of positive (e.g., disease-related) and negative edges, respectively. For an adjacency matrix  $\mathbf{W}$ , we assume that  $w_{ij}|e_{ij}^1 \stackrel{\text{iid}}{\sim} f_1$  and  $w_{ij}|e_{ij}^0 \stackrel{\text{iid}}{\sim} f_0$ , where  $f_1$  and  $f_0$  are two probability density functions with means and variances  $(\mu_1, \sigma_1^2)$  and  $(\mu_0, \sigma_0^2)$ , respectively. In addition, let  $\mathcal{M}^*$  be the true membership of edges (the community index of edges falling in sub-area pair  $(U_c, V_d)$ ). Furthermore, let  $\hat{\mathcal{M}}_{(\hat{C}, \hat{D})}$  be the membership

estimated by function (1) with  $\hat{C}$  sub-areas in Region A and  $\hat{D}$  sub-areas in Region B.

**Lemma 1. (Consistency with known sub-area numbers  $C^*$  and  $D^*$ ).** Assume that  $\mathbb{E}(\mathbf{W}\mathbf{W}^T)$  is of rank  $C^*$  with smallest absolute nonzero eigenvalue of at least  $\Lambda_A$ , and  $\mathbb{E}(\mathbf{W}^T\mathbf{W})$  is of rank  $D^*$  with smallest absolute nonzero eigenvalue of at least  $\Lambda_B$ . Assume further that  $\max(\mu_0, \mu_1, \sigma_0^2, \sigma_1^2) \leq d$  for some  $d \leq \max(\log n/n, \log m/m)$ . Then, if there exists  $(2 + \varepsilon_A) \frac{ndCD}{\Lambda_A^2} < \tau_A$  and  $(2 + \varepsilon_B) \frac{mdCD}{\Lambda_B^2} < \tau_B$  for some  $\tau_A, \tau_B, \varepsilon_A, \varepsilon_B > 0$ , the output  $\hat{\mathcal{M}}_{(\hat{C}, \hat{D})}$  that maximizes function (1) is consistent to the true membership  $\mathcal{M}_{(C^*, D^*)}^*$  underlying the latent community structure up to a permutation.

Equivalently, let  $\hat{S}_c, \hat{S}_d$  be the estimated node sets for the subgraphs  $G_c, G_d$  (induced by  $U_c$  and  $V_d$ ), respectively. Then  $\hat{S}_c \cap U_c$  represents the nodes in  $G_c$  whose assignments can be guaranteed.  $\hat{S}_d \cap V_d$  follows the same definition. With probability at least  $1 - \max(n, m)^{-1}$ , up to a permutation, we have

$$\sum_{c=1}^C \sum_{d=1}^D \left[ 1 - \frac{|\hat{S}_c \cap U_c \otimes \hat{S}_d \cap V_d|}{|U_c| |V_d|} \right] \leq \tau_A^{-1} (2 + \varepsilon_A) \frac{ndCD}{\Lambda_A^2} + \tau_B^{-1} (2 + \varepsilon_B) \frac{mdCD}{\Lambda_B^2},$$

where  $\otimes$  denotes the edge set that connects two node sets on its left and right side.

**Theorem 1. (Consistency for grid-searched  $C, D$ ).** Let the sizes of subgraph pairs  $|U_c| \times |V_d| (\forall c = [C^*], d = [D^*])$  be generated from a multinomial distribution with probabilities  $\pi = (\pi_1, \dots, \pi_{C^* \times D^*})$ . Assume  $\exists \delta > 0$ , such that

$$\mu_1 > \mu_0 \frac{1 + \delta}{1 - \delta} \left( 1 + \sqrt{1 + \frac{\pi_{\min}^2}{\pi_1^2 + \dots + \pi_{C^* \times D^*}^2}} \right),$$

then under conditions in Lemma 1 and tuning parameter  $\lambda = 0.5$ , the number of mis-assigned edges  $N_{\text{edge}}$  satisfy

$$N_{\text{edge}} = o_p(n_{\min} * m_{\min}) \text{ as } |U|, |V| \rightarrow \infty,$$

where  $n_{\min}, m_{\min}$  are the sizes of the smallest possible subgraphs in  $U$  and  $V$ , respectively.

**Theorem 2. (Convergence of Algorithm 1).** Let  $\tilde{U} = \bigoplus_{c=1}^{\tilde{C}} U_c, \tilde{V} = \bigoplus_{d=1}^{\tilde{D}} V_d$  be the partitions yielded by ratio-cut spectral clustering on  $\mathbf{W}_A$  and  $\mathbf{W}_B$  that maximizes function (1) with cluster numbers  $\tilde{C}, \tilde{D}$ . Then  $\tilde{U}, \tilde{V}$  converge almost surely to the true community structure where false-positive edge assignments to each sub-bicluster are negligible.

*Proof.* Proofs of Lemma 1 and theorems 1 and 2 are provided in Appendix B.

In summary, the above results provide theoretical evidence that the solution of the proposed objective function (1) and Algorithm 1 converge to the target community structure  $(\{U_c, V_d\})$ . Moreover, extensive simulation analyses in multiple settings with a wide range of different sample sizes demonstrate that SCCN can accurately reveal the true community structure with low false-positive and false-negative rates.

### 2.2.3 Determining $g(r)$ and $\lambda$

**Determining  $g(r)$ .** Following (Efron, 2012), we can choose  $g(\cdot)$  to be a discrete distribution on thresholds  $\{r_1, \dots, r_p\}$ . A simple example would be as follows. Suppose that the voxel-pair-level FDRs yielded by pre-selected thresholds  $r_1$ ,  $r_2$ , and  $r_3$  are 0.20, 0.10, and 0.05, respectively. We can then assign a higher probability mass to  $r_p$  that yields a lower FDR, for example,  $g(r_1) = 0.1$ ,  $g(r_2) = 0.3$ , and  $g(r_3) = 0.6$ . In addition,  $r_1$ ,  $r_2$ , and  $r_3$  can be chosen from commonly used thresholds in MRI studies, such as  $-\log(0.005)$  and  $-\log(0.001)$  ( $W_{ij}$  is  $-\log p_{ij}$  after screening, and  $r$  is a threshold for  $W_{ij}$ ).

**Selecting  $\lambda$ .** As aforementioned, the tuning parameter  $\lambda$  adjusts the balance between the subgraph size and the connection density; it thus plays a critical role in our method. A large  $\lambda$  encourages large  $|U_c|$  and  $|V_d|$ , whereas a small  $\lambda$  is stricter on the connection densities of  $(U_c, V_d)$  pairs. Essentially, the selection of  $\lambda$  is related to the network structure of  $\beta_{ij}$ . In practice, we have observed from many datasets that the coefficient  $\beta_{ij} \neq 0$  usually exhibits a block model. To reflect this, we assume the following hierarchical model. Suppose there exists a non-random, latent hyperparameter  $\beta \in \mathbb{R}^{n \times m}$  with all nonzero elements. We can generate a bipartite similarity matrix  $\eta \in \{0, 1\}^{n \times m}$  from a bipartite stochastic block model with blocks  $\{(U_c, V_d)\}$  and the corresponding connection probabilities  $\{\pi_{ij}\}$ , such that  $\eta_{ij} \sim \text{Bernoulli}(\pi_{ij})$  are independent of each other, where

$$\pi_{ij} = \begin{cases} \pi_{cd}(\lambda) & i \in U_c, j \in V_d, \\ \pi_0(\lambda) & \text{otherwise.} \end{cases}$$

We select the  $\lambda$  value that maximizes the likelihood for this block model. In practice, the  $\eta_{ij}$  values are not directly observable, and we replace them by  $\eta_{ij}(r_0) := I(w_{ij} > r_0)$ . The log-likelihood function for  $\lambda$  is:

$$l_\lambda(\pi_{cd}, \forall c \in [C], d \in [D] | \eta_{ij}(r_0)) = \sum_{c,d} \sum_{(i,j) \in U_c \times V_d} \eta_{ij}(r_0) \log \pi_{cd} + (1 - \eta_{ij}(r_0)) \log (1 - \pi_{cd}).$$

To eliminate the arbitrariness in choosing the threshold  $r_0$ , we integrate the likelihood function with respect to  $r_0$  over a prior distribution  $g_0(r_0)$  determined by the method above. This yields the following criterion:

$$\lambda_{\text{optimal}} = \operatorname{argmax}_\lambda \left\{ \int \max_{U_c, V_d, \pi_{cd}} l'_\lambda(\pi_{cd}(\lambda), \forall c = [C], d = [D] | \eta_{ij}(r_0)) g_0(r_0) dr_0 \right\}.$$

We formally present the procedure to select the tuning parameter  $\lambda$  in Algorithm 2. The overall complexity of the algorithm is  $O(Knm)$ , where  $K$  is a sufficient searching range for  $\lambda$ ,  $n = |U|$ , and  $m = |V|$ . Since the inference results between clinical groups across  $S$  subjects are captured in  $\mathbf{W}$ , the algorithm complexity no longer involves sample size  $S$ , indicating the scalability of SCCN for large datasets. In addition, clustering algorithms typically involve computing the first  $K$  eigenvectors of a potentially high-throughput similarity matrix. Our input similarity matrix  $\mathbf{W}$  is sparse after applying screening and the spatial-contiguity constraints (usually only 0.2%–5.0% of edges are non-zero entries after processing), which notably reduces computational expense. It is, however, worth noting

that since our algorithm is based on a single region pair, the computational burden may become heavy when investigating multiple different pairs, especially when a whole-brain analysis is needed.

---

**Algorithm 2** Grid search for  $\lambda$ .

---

```

1: procedure ALGORITHM
2:   for  $0 \leq \lambda \leq 1$  do
3:     return  $U = \bigoplus_{c=1}^C U_c$  and  $V = \bigoplus_{d=1}^D V_d$  by Algorithm 1
4:     for  $r_0 = (r_0)_1$  to  $(r_0)_q$  do
5:       Compute the log-likelihood:  $l_\lambda(\hat{\pi}_{c \times d}^{\text{MLE}}, \forall c = [C], d = [D] \mid \eta_{ij}(r_0))$ 
6:     end for
7:     Integrate the log-likelihood w.r.t.  $r_0$ :
8:      $l_\lambda = \sum_{i=1}^p L_\lambda(\hat{\pi}_{c \times d}^{\text{MLE}}, \forall c = [C], d = [D] \mid \eta_{ij}(r)) \ g((r_0)_i)$ 
9:   end for
10:  return  $\hat{\lambda}$  that yields maximized  $l_\lambda$ 
11: end procedure

```

---

### 2.3 Statistical inference of $\{(U_c, V_d)\}$ pairs

Recall that our ultimate goal is to extract a few most-densely connected subgraph pairs from  $\{(U_c, V_d)\}$  based on the block partition  $\{U_c, V_d : c \in [C], d \in [D]\}$  that we have already obtained at this point. A natural idea is to inspect each  $(U_c, V_d)$  pair and perform a statistical test on them with the alternative hypothesis that the subgraph  $U_c \otimes V_d$  is unusually dense. Here, we devise a cluster-wise permutation test (Nichols and Holmes, 2002) with FWER control. The hypotheses are:

$H_0$  : Subgraph  $U_c \otimes V_d$  is not unusually dense,

$H_a$  : Subgraph  $U_c \otimes V_d$  is unusually dense.

More specifically, under  $H_0$ , the connection density of  $U_c \otimes V_d$  should be close to the density of sub-area pairs obtained by randomly shuffling edges in the bipartite graph. Similar to (Grünwald, 2007), we devise the following minimum description length (MDL) test statistic:

$$\text{MDL}(U_c, V_d) = \log_2 \left[ \binom{n}{|U_c|} \binom{m}{|V_d|} \right] + \left( \frac{1 - \mu_1^2}{2 \ln 2} - L_\zeta \right) |U_c| \times |V_d|,$$

where  $\mu_1$  is the mean value of edge-wise test statistics  $\zeta_{ij}$  for edges within  $U_c \times V_d$ , and  $L_\zeta = - \int \phi(\zeta_{ij}) \log_2(\phi(\zeta_{ij})) d\zeta_{ij} + C$  is an information entropy measure based on the standard normal distribution  $\phi$  for  $\zeta_{ij}$ . Detailed derivations for the MDL-based test statistic and its connections to our inference goal are provided in Appendix B.4. We formally present the cluster-wise permutation test for each observed sub-area pair  $(U_c, V_d)$  in Algorithm 3. The number of permutations  $H$  in this algorithm can be determined based on the sample size, the targeted computational expense, and the precision of the test. For example,  $H = 1000$ .

Compared to conventional multiple testing correction methods (e.g., FDR and FWER), the MDL-based cluster-wise permutation test returns suppressed false-positive findings and shows improved statistical power in real-data examples and simulations.

---

**Algorithm 3** MDL-based cluster-wise permutation test for each  $(U_c, V_d)$  pair

---

```

1: procedure ALGORITHM
2:   Compute  $T_{c,d}^0 = \text{MDL}(U_c, V_d)$  for each  $(U_c, V_d)$  pair yielded with true covariate labels
3:   for  $h = 1, \dots, H$  do
4:     Permute covariate labels and obtain the new inference connectivity matrix  $\mathbf{W}^h$ 
5:     Obtain  $U^h = \bigoplus_{c=1}^C U_c^h$  and  $V^h = \bigoplus_{d=1}^D V_d^h$  by substituting  $\mathbf{W}^h$  in Algorithms 1 and 2
6:     return  $T^h = \max(\text{MDL}(U_c^h, V_d^h))$ 
7:   end for
8:   Compute  $p$ -value for each observed  $(U_c, V_d)$  pair:  $P_{c,d} = \frac{\sum I(T^h > T_{c,d}^0)}{H}$ 
9:   return the significance of each observed  $(U_c, V_d)$  pair based on  $P_{c,d}$  at a predetermined  $\alpha$ -level
10: end procedure

```

---

## 3 Experiments

In this section, we apply SCCN to two real datasets to investigate the voxel-level dysconnectivity under specific clinical settings. Dataset 1 includes 330 participants from a schizophrenia (SZ) research study using fMRI data collected in Baltimore, MD. Dataset 2 contains 3269 participants from a nicotine-addiction study using fMRI data collected from the UK Biobank database.

### 3.1 Schizophrenia research study

Our primary dataset contains 330 individuals, including 148 SZ patients (M/F 84/64, age  $37.5 \pm 14.4$ ) and 182 healthy controls (M/F 80/102, age  $37.0 \pm 16.1$ ). The participants were required for a large ongoing study of the effects of cognitive deficits in SZ. Specifically, the study probed how cognitive deficits contributed to functional disability in SZ patients and how they were related to altered functional networks that serve cognition. All subjects were assessed at local research centers in the greater Baltimore area between 2004 and 2016 using uniform recruitment criteria, and neurological and clinical assessments. Detailed information about participant demographics, the recruitment process, imaging acquisition, and fMRI preprocessing procedures can be found in Appendix C.1.

### 3.1.1 Saliency network disrupted connectivity

**Clinical background** The saliency network, which is mainly composed of the bilateral insula and cingulate cortices, is related to several core SZ symptoms. A vast amount of literature in neuroimaging research suggests that the connectivity in the saliency network is disturbed during information processing in SZ patients (Palaniyappan et al., 2012). We therefore intend to focus on the bilateral insula and cingulate cortices and study the schizophrenic-altered vFC patterns between them. Specifically, we want to extract schizophrenic-impacted edges that connect voxels from spatially coherent sub-areas within the insula to those within the cingulate cortex. This data-driven extraction of sub-areas caused by vFC abnormality in SZ may provide insights for more effective clinical treatments (e.g., by transcranial magnetic stimulation or deep-brain-stimulation therapies).

We labeled the bilateral insula and cingulate cortices based on the Brainnetome Atlas (Fan et al., 2016) (left insula: 1762 voxels; right insula: 1577 voxels; cingulate cortex: 5768 voxels). We first calculated the vFC matrix between the left/right insula and cingulate cortex for each subject. Each entry in the vFC matrix was a Fisher’s  $z$ -transformed Pearson correlation coefficient. Next, we obtained the population-level statistical inference matrices  $\mathbf{W}_{1762 \times 5768}^L$  and  $\mathbf{W}_{1577 \times 5768}^R$  across all subjects; each entry in  $\mathbf{W}^L$  and  $\mathbf{W}^R$  is endowed with a negative  $\log p$ -value quantifying the evidence of vFC differences between the SZ and healthy control groups. We then applied SCCN and the MDL-based test to  $\mathbf{W}^L$  and  $\mathbf{W}^R$  to respectively extract aberrant sub-area pairs between the left/right insular and cingulate cortex with the spatial-contiguity constraints. Lastly, we compared the results with those obtained using popular existing methods.

**Network-level results** Each element in the vFC inference matrix  $\mathbf{W}^L$  is  $\mathbf{W}_{ij}^L = -\log(p_{ij}^L)$ , where  $p_{ij}^L$  is the  $p$ -value testing the case-control vFC difference for the  $(i, j)$  pair between the left insula and cingulate cortex (Figure 3(L1)). We then perform screening on  $\mathbf{W}^L$  using a pre-selected threshold (e.g.,  $p = 0.05$ ):  $\mathbf{W}_{ij}^L = (\mathbf{W}^L)_{ij} \cdot I((\mathbf{W}^L)_{ij} \leq -\log(0.05))$ . The post-screened inference matrix  $\mathbf{W}^L$  can effectively exclude most non-informative false-positive edges while maintaining a high proportion of true-positive edges (Fan and Lv, 2008; Li et al., 2012b). Similar settings apply to  $\mathbf{W}^R$  (Figure 3(R1)). Implementing Algorithm 2 returned a maximum-likelihood estimation (MLE) of  $\hat{\lambda}_L = 0.625$  for  $\mathbf{W}^L$  and  $\hat{\lambda}_R = 0.75$  for  $\mathbf{W}^R$ .

Given the estimated  $\hat{\lambda}$ , Algorithm 1 returned the number of clusters  $\hat{C}_L = 135$ ,  $\hat{D}_L = 107$  for  $\mathbf{W}^L$ , and  $\hat{C}_R = 225$ ,  $\hat{D}_R = 226$  for  $\mathbf{W}^R$ . The MDL-based test returned nine abnormal sub-area pairs for  $\mathbf{W}^L$  and ten abnormal sub-area pairs for  $\mathbf{W}^R$  (marked in red in Figure 3(L2) and (R2)). A 3D demonstration of the detected results from  $\mathbf{W}^L$  is shown in Figure 4 (using a significance level of 0.05 from the MDL-based permutation test). Information regarding the precise sizes,  $p$ -values, and locations is also specified in Figure 4. All extracted sub-area pairs show well-organized topological structures. Overall, the aberrant vFC patterns from  $\mathbf{W}^L$  are gathered between the dorsal insula and anterior cingulate cortex (ACC). Detailed detection results for  $\mathbf{W}^R$  are provided in Appendix C.2.

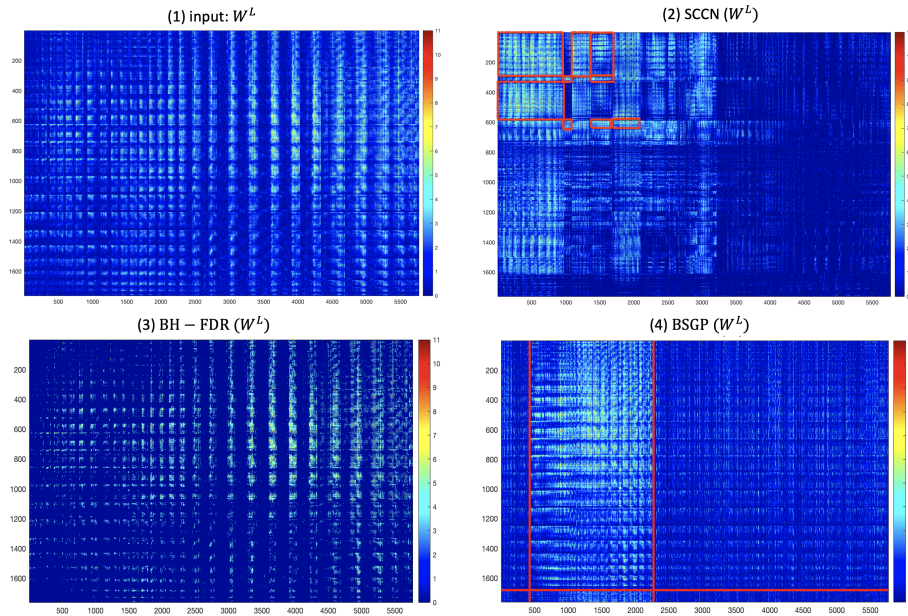


Figure 3: (1) A heatmap of  $W^L$ : rows and columns correspond to the voxels from the left insula and the cingulate cortex, respectively. A hotter entry indicates a more differentially expressed voxel pair between clinical groups adjusted for other covariates. (2) Results yielded by SCCN: positive sub-area pairs that pass the MDL-based permutation test are highlighted in red boxes. There are many edges with small  $p$ -values outside the red boxes (e.g., in the bottom left corner) because they are not spatially contiguous to those inside the boxes, and are automatically excluded by SCCN. (3) Results yielded by BH-FDR: with  $q = 0.05$ , no sub-area pairs were detected. (4) Results yielded by BSGP: only one informative yet much less dense sub-area pair was detected. The detected sub-area pair was also lack of spatial contiguity and specificity.

**Biological interpretation of detected sub-areas** The detected sub-areas consist of several well-known brain regions that are believed to be frequently associated with SZ disorder, including, most remarkably, the anterior insula (AI) and ACC. Emotions that most strongly engage the AI, such as anger and fear, are those that SZ patients tend to have the most difficulty recognizing (Wylie and Tregellas, 2010). Furthermore, the densities of neurons, axons, and synapses are found to be abnormal in the ACCs of people with SZ (Arnold and Trojanowski, 1996). All of the aberrant edges detected showed decreased or equivalent connections in SZ patients. This aligns with medical findings that SZ is a “dysconnectivity” disorder with primarily reduced FC across the salience network (Lynall et al., 2010), although medication effects cannot be completely ruled out. The imposed spatial-contiguity constraints help unfold brain sub-areas of the bilateral insula and cingulate cortices that maximally cover disease-related vFC. These novel findings improve the spatial specificity of SZ-related dysconnectivity in the well-known salience network and may lead to guidance for future treatments.

**Comparisons with existing methods** For comparison purposes, we performed the Benjamini–Hochberg FDR (BH-FDR) correction edge-wisely and a commonly used biclus-

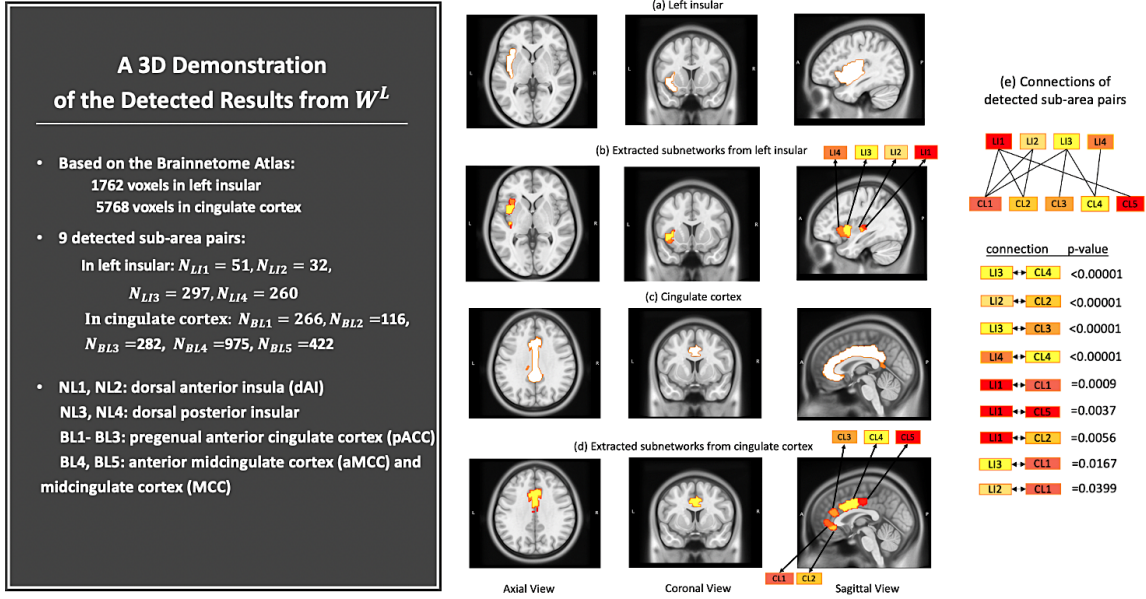


Figure 4: A 3D demonstration of the detected sub-area pairs from  $W^L$ . Let  $LI_i$  be the  $i$ -th dysconnected sub-area detected from the left insula that is connected to the  $j$ -th sub-area from the cingulate cortex,  $CL_j$ . Let  $N_{LI_i}$  denote the number of voxels in sub-area  $LI_i$ , and similarly  $N_{CL_j}$  for  $CL_j$ . (a)(c) show the images of the original left insular and cingulate cortex; (b) shows the SZ-affected sub-areas in the left insular that are connected to those in the cingulate cortex highlighted in (d); (e) shows the architecture of interconnections between the detected sub-areas from  $W^L$  and the associated  $p$ -values from the MDL-based permutation test. A 3D demonstration of the detected results from  $W^R$  is provided in Appendix C.2.

tering algorithm, bipartite spectral graph partitioning (BSGP), cluster-wisely. By first conducting an initial correlation analysis between vFC and schizophrenic status, 17.84% of the edges in  $W^L$  were found to have  $p < 0.005$  significance, where  $p = 0.005$  is a commonly used yet uncorrected threshold in neuroimaging studies (Derado et al., 2010). After applying BH-FDR correction, 9.45% of the edges were found to be significant using the threshold of  $q = 0.01$  (Figure 3(L3)), and no community structure was revealed. For  $W^R$ , 13.50% of edges had  $p$ -values less than 0.005, and only 3.61% significant edges were found after BH-FDR correction with  $q = 0.01$  (Figure 3(R3)); again, no community structure was found in  $W^R$ . When applying BSGP to both  $W^L$  and  $W^R$ , only one abnormal sub-area pair was detected (Figure 3(L4) and (R4)), with more than 36.80% edges of  $p > 0.005$  included compared to SCCN. In comparison to the existing methods, SCCN yields much more densely schizophrenia-associated vFC contained in spatially contiguous sub-area pairs with stronger topological structures.

### 3.1.2 Temporal-thalamic disrupted connectivity

In contrast to the reduced salience network connections in SZ patients, many studies have shown that SZ patients have greater thalamic connectivity with multiple sensory-motor regions, including, most remarkably, the temporal gyrus (Ferri et al., 2018; Cetin et al.,



2014). More specifically, thalamus to middle temporal gyrus connectivity was positively correlated with many core SZ features, such as hallucinations and delusions. We therefore aim to use SCCN to identify some novel findings between the middle temporal gyrus on the right hemisphere and the bilateral thalamus in SZ patients. Based on the Brainnetome Atlas, there are 3566 voxels in the right middle temporal gyrus (labeled 82, 84, 86, and 88) and 3275 voxels in the bilateral thalamus (labeled 231–246). We computed the vFC connectivity inference matrices  $\mathbf{W}_{3566 \times 1727}^{(\text{Tem}_{\text{right}}, \text{Tha}_{\text{left}})}$  and  $\mathbf{W}_{3566 \times 1548}^{(\text{Tem}_{\text{right}}, \text{Tha}_{\text{right}})}$  between clinical groups and then implemented SCCN. Due to limited space here, we provide the results for the selections of all parameters and densely altered sub-area pairs in Appendix C.3.

## 3.2 Nicotine-addiction research study

Our primary dataset contains 3269 individuals from the UK Biobank database, including 1353 constant current smokers (M/F: 2653/616, age:  $48.6 \pm 15.3$ ) and 1916 previous light smokers (M/F: 1187/729, age:  $32.9 \pm 18.1$ ). Specifically, we define current smokers as participants who currently smoke more than ten cigarettes per day (i.e., cases who are addicted to nicotine). We define previous light smokers as those who indicated that they had only tried a few cigarettes in the past but are not currently addicted to nicotine products (i.e., controls). By investigating different neural-connectivity patterns across the two groups, we may obtain more information on the inherent neurological mechanism of nicotine dependence and thereby help smokers resist nicotine cravings.

### Clinical background

Abundant literature shows that the basal ganglia (BG), hippocampus (Hippo), and insular gyrus (Ins) play important roles in nicotine addiction (Ersche et al., 2011; Gaznick et al., 2014; McClernon et al., 2016). We therefore intend to look into the disrupted connectivity patterns between all possible pairs (12 in total) formed by these three bilateral ROIs: (BG, Hippo), (BG, Ins), and (Hippo, Ins). To keep the presentation concise, we will present the results of the (left BG, left Ins) pair here and the remaining 11 cases in Appendix D. Again, we labeled the left BG and left Ins using the Brainnetome Atlas (left BG: 2345 voxels; left Ins: 1762 voxels). We followed the same computational procedures as in Dataset 1 and obtained the edge-wise connectivity inference matrices  $\mathbf{W}_{2345 \times 1762}^{(\text{BG}_{\text{left}}, \text{Ins}_{\text{left}})}$  across clinical groups. We then applied SCCN and the MDL-based test to  $\mathbf{W}^{(\text{BG}_{\text{left}}, \text{Ins}_{\text{left}})}$  to extract abnormal sub-area pairs with the spatial-contiguity constraints. Lastly, we compared the results with those obtained using two common existing methods.

### Network-level results

Each entry in the inference matrix  $\mathbf{W}^{(\text{BG}_{\text{left}}, \text{Ins}_{\text{left}})}$  is endowed with a  $-\log p$  value testing the vFC difference between clinical groups. (Figure 5(1)). Implementing Algorithm 2 returned the MLE  $\hat{\lambda} = 0.75$ . Given the estimated  $\hat{\lambda}$ , Algorithm 1 returned the number of clusters  $\hat{C} = 306$ ,  $\hat{D} = 210$  for  $\mathbf{W}^{(\text{BG}_{\text{left}}, \text{Ins}_{\text{left}})}$ . The MDL-based test returned six abnormal

sub-area pairs, which are marked in red in [Figure 5\(2\)](#). A 3D demonstration of the detected sub-area pairs from  $\mathbf{W}^{(\text{BG}_{\text{left}}, \text{Ins}_{\text{left}})}$  is shown in [Figure 5\(a\)–\(e\)](#) (with a significance level of 0.05 selected for the MLD-based permutation test). All extracted sub-area pairs show well-organized topological structures. The majority of aberrant vFC patterns from  $\mathbf{W}^{(\text{BG}_{\text{left}}, \text{Ins}_{\text{left}})}$  are gathered between the medial inferior part of the left basal ganglia and the left insula.

### Biological interpretation of detected sub-areas

The detected sub-areas consist of several locations that are believed to be frequently associated with nicotine addiction, including the medial inferior part of the basal ganglia and the posterior insula. We also observed decreased connectivity within these regions in current smokers, which aligns with the previous medical discovery that decreased resting-state functional connectivity is correlated with increased nicotine-addiction severity ([Fedota and Stein, 2015](#); [Sutherland and Stein, 2018](#)). The incorporated spatial-contiguity constraints help unfold the sub-areas within the BG, Hippo, and Ins, which maximally cover addiction-related vFC. These novel findings improve the spatial specificity of addiction-related locations in the three brain regions and may lead to future guidance for resisting the urge to use nicotine products.

### Comparisons with existing methods

For comparison purposes, we again performed the BH-FDR correction edge-wisely and BSGP cluster-wisely on  $\mathbf{W}^{(\text{BG}_{\text{left}}, \text{Ins}_{\text{left}})}$ . By first conducting an initial edge-wise significance test across the current and previously light smoker groups, only 7.29% of the edges were found to be significant ( $p < 0.005$ ). However, no edges showed significance after applying BH-FDR correction with  $q = 0.01$  ([Figure 5\(3\)](#)). When applying BSGP to  $\mathbf{W}^{(\text{BG}_{\text{left}}, \text{Ins}_{\text{left}})}$ , only one abnormal sub-area pair was detected ([Figure 5\(4\)](#)), with 49.5% edges of  $p > 0.005$  included in the detected pair, compared to 3.12% yielded by SCCN. In comparison to the two existing methods, SCCN yields much more densely altered vFC contained in spatially contiguous sub-area pairs with strong topological structures.

## 4 Simulations

In the simulation study, we probed whether SCCN can extract densely altered sub-area pairs with better performance compared to common existing methods. Specifically, we evaluated the performance from two perspectives. (i) Multivariate edge-level inference: whether extracted voxel pairs have a high true-positive rate (TPR) and low false-positive rate (FPR); (ii) network-level inference: whether the extracted sub-areas contain maximal true-positive voxels, compared to other unextracted sub-areas.

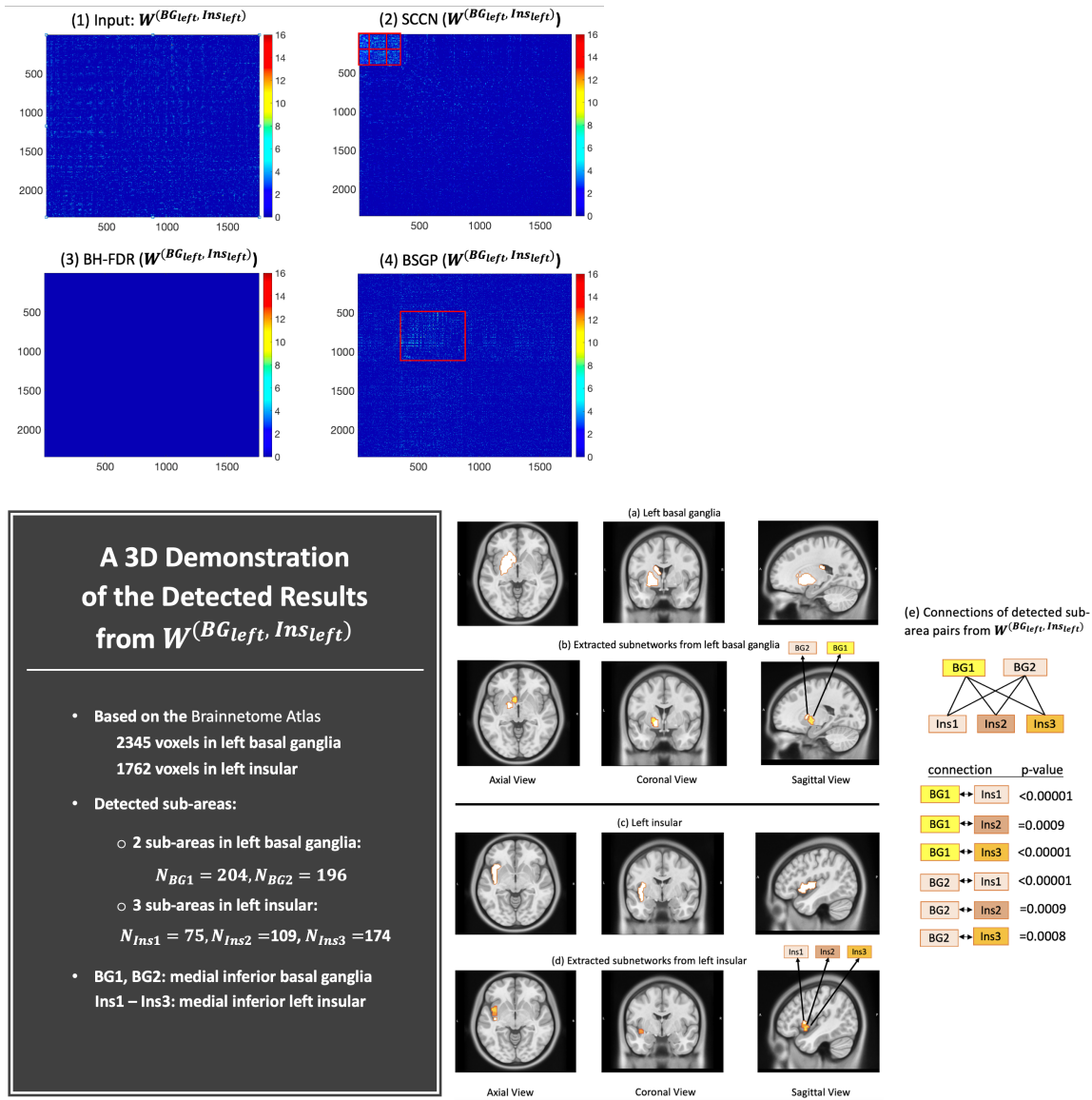


Figure 5: (1) A heatmap of  $W^{(BG_{left}, Ins_{left})}$ : rows and columns correspond to voxels from the left basal ganglia and the left insular, respectively. (2) Results yielded by SCCN: altered sub-area areas that pass the MDL-based permutation test are highlighted in red boxes. (3) Results yielded by BH-FDR: The hypothesis testing error measure was set to be  $q = 0.05$  as a cut-off. No sub-area pairs were detected. (4) Results yielded by BSGP: only one positive yet much less dense sub-area pair was detected. The detected sub-area pair also lack spatial contiguity and specificity. (a)-(d) shows the 3D demonstration of the 6 detected altered sub-areas from  $W^{(BG_{left}, Ins_{left})}$ . (a)-(e) show a 3D demonstration of the detected results from  $W^{(BG_{left}, Ins_{left})}$ . Based on the p-values from the MDL-based permutation test shown in (e), most positive sub-area pairs are located in the medial inferior part of left basal ganglia and left insular.

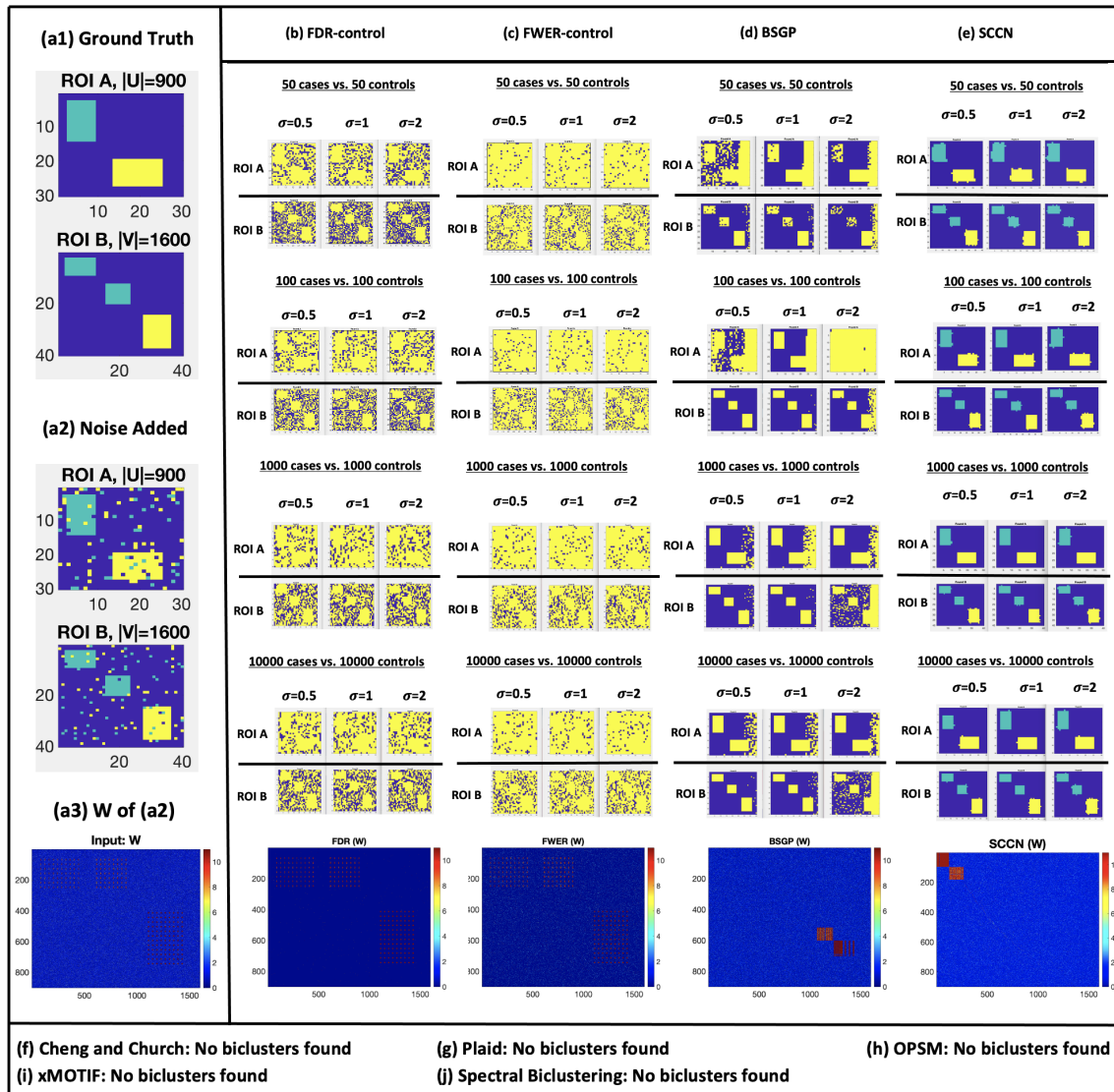


Figure 6: Visualization of simulation results. (a1) shows the ground truth locations of the disease-related sub-area pairs  $(U_1, V_1)$ ,  $(U_1, V_2)$ , and  $(U_2, V_3)$  with spatial contiguity (only regions with same color exhibit dysconnectivity from A to B). (a2) includes additional noise and positive but isolated voxel pairs based on (a1) to mimic the real vFC patterns in the brain connectome. (a3) shows the connectivity inference matrix  $\mathbf{W}$  obtained based on (a2). (b)-(e) show the detected disease-related voxel pairs (again only regions with the same color form a pair) under different variances  $\sigma$  and sample sizes  $S$ . The last row shows the isomorphic graphs of (a3) with the extracted sub-area pairs pushed to the top. We highlight the voxels from the supra-threshold voxel pairs that were yielded by the FDR-control and FWER-control, and voxels in sub-area pairs that were extracted by BSGP and SCCN. Multiple testing with FDR-control and FWER-control tend to extract an excess of voxels with high false-positive error rates. BSGP better controls the error rates, but it extracts voxel pairs without differentiating the correct area-wise connections, i.e.,  $(U_1, V_1)$ ,  $(U_1, V_2)$ , and  $(U_2, V_3)$ . In contrast, SCCN can simultaneously recover the spatially-contiguous sub-areas, respectively, in A and B, and reveal the correct disease-related vFC patterns. (f)-(j) show that no single differentially expressed sub-area pair was extracted by the biclustering algorithms listed.

## 4.1 Primary analysis

We first generated a bipartite graph  $G = \{U, V\}$  to represent the brain connectome between two brain regions A and B for  $S$  subjects (Figure 6(a1)), where  $U$  corresponds to the voxel set in Region A, and  $V$  corresponds to that in Region B. We assume all  $S$  subjects share common node sets after spatial normalization and registration, i.e.,  $(U^s, V^s) \equiv (U, V), \forall s \in [S]$ . Next, we simulated covariates of interest  $\{\mathbf{X}^1, \dots, \mathbf{X}^S\}$  that contain clinical information of all  $S$  subjects. Lastly, we simulated the Fisher’s  $z$ -transformation connectivity matrices  $\{\mathbf{Z}^1, \dots, \mathbf{Z}^S\}$  between regions A and B for all subjects, where  $\mathbf{Z}^s \in \mathbb{R}^{n \times m}, n = |U|, m = |V|$ . Specifically, each element  $z_{ij}^s$  in  $\mathbf{Z}^s$  was set to follow  $\mathcal{N}(h(z_{ij}^s), \sigma^2)$ , where  $h(z_{ij}^s) = \mathbf{X}^s \beta_{ij}$  is location-specific within regions A and B.

In the following, we show the numerical settings under the above simulation framework:

1. For the two pre-defined brain regions of interest, we simulated  $|U| = 900$  voxels in Region A and  $|V| = 1600$  voxels in Region B. Within  $|U|$  and  $|V|$ , we also randomly simulated three disease-related sub-area pairs  $(U_1, V_1)$ ,  $(U_1, V_2)$ , and  $(U_2, V_3)$ . Not every possible pair  $\{(U_c, V_d), c = [2], d = [3]\}$  was associated with the disease; only regions with the same color exhibited dysconnectivity from A to B (see Figure 6(a1)). The sizes of these sub-area pairs were  $|U_1||V_1| = 84 \times 70 = 5880$ ,  $|U_1||V_2| = 84 \times 64 = 5376$ , and  $|U_2||V_3| = 96 \times 117 = 11\,232$ . In addition, we included spatially isolated abnormal voxels as well as noise within regions A and B to mimic more realistic neural connectivity (Figure 6(a2)).
2. For the Fisher’s  $z$ -transformation connectivity matrices  $\{\mathbf{Z}^s, s \in S\}$ , we set  $h(z_{ij}^s) = \beta_0 + \beta_{ij,1}x_1^s + \beta_{ij,2}x_2^s + \beta_{ij,3}x_3^s$ , where  $x_1^s$  and  $x_2^s$  store the age and sex information for subject  $s$ , and  $x_3^s$  represents their clinical status ( $x_3^s=1$  if patient  $s$  has a mental disorder, and 0 for a healthy control.). In addition, while  $\beta_{ij,1}$  and  $\beta_{ij,2}$  are typically not spatially variant,  $\beta_{ij,3}$  is considered brain-region specific:

$$\beta_{ij,3} = \begin{cases} 0.9, & \text{if } (i, j) \in (U_1, V_1) \cup (U_1, V_2), \\ 0.13, & \text{if } (i, j) \in (U_2, V_3), \\ 0, & \text{if } (i, j) \in U / \{(U_1, V_1) \cup (U_1, V_2) \cup (U_2, V_3)\}. \end{cases}$$

3. To control standardized effect sizes, we set  $\sigma^2 = 0.5, 1.0, 2.0$  in  $\mathbf{Z}^s \sim \mathcal{N}(h(z_{ij}^s), \sigma^2)$ . Additionally, four sample sizes,  $S = 100, 200, 2000$ , and  $20,000$ , were used, each with balanced healthy controls and patients. All settings with different  $(\sigma, S)$  were simulated for 1000 times to assess the variability of the TPR and FPR.

We implemented Algorithm 1 and 2 of SCCN to identify sub-area pairs from each simulated dataset, and we then applied Algorithm 3 to conduct cluster-wise inference on the sub-area pairs detected. To assess the performance of the multivariate edge-wise inference, we considered two conventional multiple-testing controls (FDR and FWER). Specifically, we used the voxel-wise permutation test (with 1000 permutations) to control the FWER and the Benjamini–Hochberg procedure (with  $q = 0.05$  as a cut-off) to control the FDR (Benjamini and Hochberg, 1995). To assess the accuracy of the cluster-wise

performance, our goal was to compare true disease-related subgraphs  $\{(U_c, V_d)\}$  with the estimated subgraphs  $\{(\hat{U}_c, \hat{V}_d)\}$  produced by five commonly used biclustering algorithms (i.e., Cheng and Church, Plaid, OPSM, xMOTIF, and Spectral Biclustering (J. K. Gupta, 2013)).

The edge-wise inference results are presented in Table 1, and a graph illustration of the results is shown in Figure 6. For the edge-wise inference performance with all different  $(\sigma, S)$ , SCCN outperforms the two traditional multiple testing correction methods (i.e., FDR and FWER control) in terms of TPR, while its ability to control the FPR falls in between the two. SCCN’s relatively inferior performance in controlling the FPR (compared to sensitivity) can sometimes be impacted by the following disadvantage: in traditional multiple testing methods with universal thresholds, one false-positive finding corresponds to exactly one false-positive edge. However, SCCN detects altered edges by partitioning voxels within each ROI; therefore, one false-positive finding by SCCN corresponds to one false-positive voxel, say  $v_i \in U_c$ , which will lead to  $n$  false positive edges when  $V_d$  ( $|V_d| = n$ ) is found to connect to  $|U_c|$ . The greater the size of  $V_d$ , the more false-positive edges will be yielded. Nonetheless, even with such a heavy penalty for detecting one false-positive voxel, SCCN still controls the FPR and shows better performance when jointly considering the TPR and FPR. More importantly, false-positive edges discovered by the traditional FDR and FWER correction approaches almost cover all within-ROI voxels, which leads to a substantial loss of spatial specificity when identifying covariate-related vFC patterns.

Regarding the network-level inference performance, all common biclustering methods failed to detect any positive biclusters (differentially expressed sub-area pairs) except for BSGP. However, BSGP nonetheless failed to ensure spatial contiguity, and the precise connection between the extracted sub-areas was not correctly revealed. That is, unlike the results yielded SCCN (Figure 6(e)), BSGP (Figure 6(d)) could not effectively differentiate between yellow and blue clusters. In comparison, SCCN shows outstanding network-level performance for detecting community structures and incorporating spatial contiguity.

## 4.2 Negative control analysis

We further performed a negative control analysis to evaluate the FPR of our method. We consider a scenario in which the connections between a pre-selected ROI pair are unrelated to a clinical condition of interest. We generated  $|U| = 900$  and  $|V| = 1600$  voxels in regions A and B. We distinguished the patient and control groups as 1 and 0, but since there were no abnormal sub-area pairs  $\{(U_c, V_d)\}$  across groups, we simply set the connectivity matrices  $\mathbf{Z}^s \sim \mathcal{N}(0, \sigma^2)$  over the entire regions for all  $S$  subjects. Based on  $\mathbf{Z}^s$ , we obtained the inference matrix  $\mathbf{W}^0$  across clinical groups. Since the network detection was validated to be scalable to different sample sizes and sample variances, we evaluated the configuration ( $S = 1000, \sigma = 1$ ) as a proof of concept. Finally, we implemented SCCN on  $\mathbf{W}^0$ . Since the false positive voxel pairs tended to be distributed randomly, no sub-area pairs were significant. Therefore, the sub-area-level false positive findings were 0. The edge-wise FPR (supra-threshold voxel-pairs) among 1000 iterations was  $6.82 \times 10^{-5}$  (std.  $1.29 \times 10^{-5}$ ), which is consistent with the pre-determined alpha level ( $\mathbb{E}(p) = 0.00005$ ). We have provided

Sample Size: 50 cases vs. 50 controls				
Methods	$\sigma$	0.5	1	2
FDR-control	TPR	0.918 (0.229)	0.832 (0.314)	0.637 (0.328)
	FPR	0.060 (0.007)	0.065 (0.053)	0.073 (0.158)
	Network Detection	No	No	No
FWER-control	TPR	0.994 (0.169)	0.893 (0.177)	0.842 (0.179)
	FPR	0.762 (0.142)	0.764 (0.152)	0.771 (0.193)
	Network Detection	No	No	No
SCCN	TPR	1(0)	1(0)	1(0)
	FPR	0.087 (0.011)	0.093 (0.012)	0.096 (0.014)
	Network Detection	Yes	Yes	Yes
BSGP	TPR	0.946 (0.106)	0.893 (0.122)	0.667 (0.278)
	FPR	0.858 (0.258)	0.773 (0.173)	0.845 (0.439)
	Network Detection	Yes	Yes	Yes
Cheng and Church Plaid OPSM xMOTIF Spectral Biclustering	TPR	0(0)	0(0)	0(0)
	FPR	0(0)	0(0)	0(0)
	Network Detection	No biclusters detected		

Sample Size: 100 cases vs. 100 controls				
Methods	$\sigma$	0.5	1	2
FDR-control	TPR	0.958 (0.215)	0.892 (0.249)	0.746 (0.427)
	FPR	0.065 (0.069)	0.069 (0.048)	0.070 (0.164)
	Network Detection	No	No	No
FWER-control	TPR	0.994 (0.157)	0.989 (0.182)	0.842 (0.163)
	FPR	0.767 (0.139)	0.762 (0.140)	0.761 (0.187)
	Network Detection	No	No	No
SCCN	TPR	1(0)	1(0)	1(0)
	FPR	0.081 (0.010)	0.082 (0.012)	0.097 (0.013)
	Network Detection	Yes	Yes	Yes
BSGP	TPR	1 (0.105)	1 (0.120)	0.993 (0.262)
	FPR	0.844 (0.228)	0.764 (0.172)	0.940 (0.369)
	Network Detection	Yes	Yes	Yes
Cheng and Church Plaid OPSM xMOTIF Spectral Biclustering	TPR	0(0)	0(0)	0(0)
	FPR	0(0)	0(0)	0(0)
	Network Detection	No biclusters detected		

Sample Size: 1000 cases vs. 1000 controls				
Methods	$\sigma$	0.5	1	2
FDR-control	TPR	0.957 (0.209)	0.878 (0.287)	0.789 (0.363)
	FPR	0.061 (0.007)	0.061 (0.058)	0.071 (0.159)
	Network Detection	No	No	No
FWER-control	TPR	0.993 (0.169)	0.904 (0.180)	0.823 (0.187)
	FPR	0.749 (0.140)	0.727 (0.145)	0.754 (0.176)
	Network Detection	No	No	No
SCCN	TPR	1(0)	1(0)	1(0)
	FPR	0.081 (0.008)	0.087 (0.010)	0.081 (0.012)
	Network Detection	Yes	Yes	Yes
BSGP	TPR	0.968 (0.106)	0.903 (0.122)	0.875 (0.278)
	FPR	0.374 (0.438)	0.405 (0.360)	0.737 (0.447)
	Network Detection	Yes	Yes	Yes
Cheng and Church Plaid OPSM xMOTIF Spectral Biclustering	TPR	0(0)	0(0)	0(0)
	FPR	0(0)	0(0)	0(0)
	Network Detection	No biclusters detected		

Sample Size: 10000 cases vs. 10000 controls				
Methods	$\sigma$	0.5	1	2
FDR-control	TPR	0.959 (0.229)	0.873 (0.357)	0.771 (0.391)
	FPR	0.060 (0.007)	0.061 (0.061)	0.069 (0.160)
	Network Detection	No	No	No
FWER-control	TPR	0.992 (0.174)	0.907 (0.176)	0.819 (0.183)
	FPR	0.753 (0.145)	0.734 (0.145)	0.759 (0.157)
	Network Detection	No	No	No
SCCN	TPR	1(0)	1(0)	1(0)
	FPR	0.081 (0.007)	0.091 (0.007)	0.087 (0.011)
	Network Detection	Yes	Yes	Yes
BSGP	TPR	0.972 (0.208)	0.884 (0.122)	0.873 (0.290)
	FPR	0.574 (0.426)	0.368 (0.499)	0.679 (0.407)
	Network Detection	Yes	Yes	Yes
Cheng and Church Plaid OPSM xMOTIF Spectral Biclustering	TPR	0(0)	0(0)	0(0)
	FPR	0(0)	0(0)	0(0)
	Network Detection	No biclusters detected		

Table 1: Simulation results. The four sub-tables show the inference results given different sample sizes and variances, where TPR and FPR correspond to the edge-wise true positive rate and false positive rate. Network detection results indicate whether the algorithm can successfully extract the correct connection patterns between disease-related sub-area pairs.

a graph visualization of these results in Appendix E.

In summary, we have shown that the sub-area detection is not affected by different values of variance  $\sigma^2$ , sample size  $S$ , or other sources of noise. SCCN also yields vFC patterns with high sensitivity and low FPRs. The spatial-contiguity constraints allow positive edges to borrow strengths from each other within a data-driven sub-area; sensitivity is thus notably increased. Data-driven sub-areas with these constraints can also exclude false-positive edges that bridge voxels that are randomly scattered in ROIs. False-positive findings are therefore largely suppressed. In addition, the jointly improved sensitivity (and thus statistical power) and control of the FPR yield almost identical voxel sets across all simulated datasets. Replicability is hence remarkably improved.

## 5 Discussion

Psychiatric and neurological disorders are often associated with a disrupted brain connectome. To improve the spatial specificity and sensitivity for detecting a disease-impacted brain connectome, in this work, we focused on voxel-level connectivity network analysis. We developed statistical models focusing on extracting abnormal voxel pairs from a region pair of interest, which can be further extended to whole-brain connectome analysis. We have attempted to simultaneously address the challenges of a controlled FPR for multiple voxel-pair testing and the spatial-contiguity constraints for vFC analysis. In fact, it is also possible that disease-related voxel-level connectivity occurs within a region. We can apply a similar approach to a pre-obtained within-region adjacency matrix  $\mathbf{W}_{n \times n}$  by integrating a corresponding spatial-contiguity infrastructure graph, say  $\mathcal{S}_A$ . Following this, SCCN becomes applicable to intra-region voxel-level connectivity analysis. We provide detailed procedures for this in Appendix A.3. In addition, the brain parcellation to extract sub-areas is usually based on commonly used brain atlases (e.g., Brodmann’s map or the International Consortium for Brain Mapping), and these were built on comprehensively studied cortical anatomy, such as complex gyro-sulcal folding patterns. Different regions blocked by gyri and sulci tend to show differential neurobiological structures and functions, and these atlases can thus serve as a good foundation to investigate sub-area community structures. However, to further overcome the limitation of using existing brain parcellations, one can consider combining any extracted spatially adjacent sub-areas from a pair of spatially adjacent regions if the combination is statistically coherent and biologically meaningful.

The centerpiece of our proposed method is the identification of sub-area pairs containing an unusually high density of phenotype-related voxel pairs. By leveraging this high density, we can effectively control the FPR by excluding isolated false-positive edges, and we thus greatly reduce the number of false-positive nodes. We have therefore improved the spatial specificity of extracted disease-related patterns at a voxel level. Herein, we have proposed a new non-parametric objective function to achieve this goal, and this has been implemented with efficient algorithms. We also developed inference methods to assess the statistical significance of each sub-area pair extracted.



The biological findings from our data example are novel; SCCN revealed vFC connectome patterns for schizophrenia within the well-known salience network. We discovered that the malfunction of salience network connectivity is mainly driven by disrupted connections between the dorsal insula and anterior cingulate cortex instead of the omnibus region-level findings. We further validated our findings through extensive simulations and showed that our methods could improve sensitivity with a controlled FPR while retaining spatial contiguity.

In summary, SCCN provides a new toolkit for vFC analysis with improved spatial resolution and specificity while preserving a well-controlled false-positive error rate. Therefore, the findings from SCCN can be translated into more effective potential treatments for brain disorders. Since the input data of SCCN is voxel-pair-level inference results, it is applicable to all connectivity measures and data modalities where valid statistical inference can be performed (e.g., white-matter tractography). SCCN may also provide a promising strategy for whole-brain connectome voxel-pair network analysis. All sample code can be found at <https://github.com/TongLu-bit/DecodingNetwork>.

## References

- Ardila, A., Bernal, B., and Rosselli, M. (2016). How localized are language brain areas? a review of brodmann areas involvement in oral language. *Archives of Clinical Neuropsychology*, 31(1):112–122.
- Arnold, S. and Trojanowski, J. (1996). Recent advances in defining the neuropathology of schizophrenia. *Acta neuropathologica*, 92(3):217–231.
- Bahrami, M., Laurienti, P. J., and Simpson, S. L. (2019). Analysis of brain subnetworks within the context of their whole-brain networks. *Human brain mapping*, 40(17):5123–5141.
- Bellec, P., Perlberg, V., Jbabdi, S., Péligrini-Issac, M., Anton, J.-L., Doyon, J., and Benali, H. (2006). Identification of large-scale networks in the brain using fmri. *Neuroimage*, 29(4):1231–1243.
- Benjamini, Y. and Hochberg, Y. (1995). Controlling the false discovery rate: a practical and powerful approach to multiple testing. *Journal of the Royal statistical society: series B (Methodological)*, 57(1):289–300.
- Bolla, M. (2013). *Spectral clustering and biclustering: Learning large graphs and contingency tables*. John Wiley & Sons.
- Boltzmann, L. (1866). *Über die mechanische Bedeutung des zweiten Hauptsatzes der Wärmetheorie:(vorgelegt in der Sitzung am 8. Februar 1866)*. Staatsdruckerei.
- Bradley, P. S. and Fayyad, U. M. (1998). Refining initial points for k-means clustering. In *ICML*, volume 98, pages 91–99. Citeseer.

- Bullmore, E. and Sporns, O. (2009). Complex brain networks: graph theoretical analysis of structural and functional systems. *Nature reviews neuroscience*, 10(3):186–198.
- Cano, C., Adarve, L., López, J., and Blanco, A. (2007). Possibilistic approach for biclustering microarray data. *Computers in biology and medicine*, 37(10):1426–1436.
- Cao, M., Wang, J.-H., Dai, Z.-J., Cao, X.-Y., Jiang, L.-L., Fan, F.-M., Song, X.-W., Xia, M.-R., Shu, N., Dong, Q., et al. (2014). Topological organization of the human brain functional connectome across the lifespan. *Developmental cognitive neuroscience*, 7:76–93.
- Cetin, M. S., Christensen, F., Abbott, C. C., Stephen, J. M., Mayer, A. R., Cañive, J. M., Bustillo, J. R., Pearson, G. D., and Calhoun, V. D. (2014). Thalamus and posterior temporal lobe show greater inter-network connectivity at rest and across sensory paradigms in schizophrenia. *Neuroimage*, 97:117–126.
- Chen, S., Bowman, F. D., and Mayberg, H. S. (2016). A bayesian hierarchical framework for modeling brain connectivity for neuroimaging data. *Biometrics*, 72(2):596–605.
- Chen, S., Bowman, F. D., and Xing, Y. (2020). Detecting and testing altered brain connectivity networks with k-partite network topology. *Computational statistics & data analysis*, 141:109–122.
- Chen, S., Wu, Q., and Hong, L. E. (2019). Graph combinatorics based group-level network inference. *bioRxiv*, page 758490.
- Chen, S., Zhang, Y., Wu, Q., Bi, C., Kochunov, P., and Hong, L. E. (2023). Identifying covariate-related subnetworks for whole-brain connectome analysis. *Biostatistics*, page kxad007.
- Cheng, H., Hua, K. A., and Vu, K. (2008). Constrained locally weighted clustering. *Proceedings of the VLDB Endowment*, 1(1):90–101.
- Craddock, R. C., James, G. A., Holtzheimer III, P. E., Hu, X. P., and Mayberg, H. S. (2012). A whole brain fmri atlas generated via spatially constrained spectral clustering. *Human brain mapping*, 33(8):1914–1928.
- Derado, G., Bowman, F. D., and Kilts, C. D. (2010). Modeling the spatial and temporal dependence in fmri data. *Biometrics*, 66(3):949–957.
- Efron, B. (2008). Microarrays, empirical bayes and the two-groups model. *Statistical science*, 23(1):1–22.
- Efron, B. (2012). *Large-scale inference: empirical Bayes methods for estimation, testing, and prediction*, volume 1. Cambridge University Press.
- Eickhoff, S. B., Thirion, B., Varoquaux, G., and Bzdok, D. (2015). Connectivity-based parcellation: Critique and implications. *Human brain mapping*, 36(12):4771–4792.

- Ersche, K. D., Barnes, A., Jones, P. S., Morein-Zamir, S., Robbins, T. W., and Bullmore, E. T. (2011). Abnormal structure of frontostriatal brain systems is associated with aspects of impulsivity and compulsivity in cocaine dependence. *Brain*, 134(7):2013–2024.
- Fan, J., Han, X., and Gu, W. (2012). Estimating false discovery proportion under arbitrary covariance dependence. *Journal of the American Statistical Association*, 107(499):1019–1035.
- Fan, J. and Lv, J. (2008). Sure independence screening for ultrahigh dimensional feature space. *Journal of the Royal Statistical Society: Series B (Statistical Methodology)*, 70(5):849–911.
- Fan, L., Li, H., Zhuo, J., Zhang, Y., Wang, J., Chen, L., Yang, Z., Chu, C., Xie, S., Laird, A. R., et al. (2016). The human brainnetome atlas: a new brain atlas based on connectional architecture. *Cerebral cortex*, 26(8):3508–3526.
- Farahani, F. V., Karwowski, W., and Lighthall, N. R. (2019). Application of graph theory for identifying connectivity patterns in human brain networks: a systematic review. *frontiers in Neuroscience*, 13:585.
- Fedota, J. R. and Stein, E. A. (2015). Resting-state functional connectivity and nicotine addiction: prospects for biomarker development. *Annals of the new York Academy of Sciences*, 1349(1):64–82.
- Feng, X. and He., X. (2014). Statistical inference based on robust low-rank data matrix approximation. *The Annals of Statistics.*, 42(1):190–210.
- Ferri, J., Ford, J., Roach, B., Turner, J., Van Erp, T., Voyvodic, J., Preda, A., Belger, A., Bustillo, J., O’Leary, D., et al. (2018). Resting-state thalamic dysconnectivity in schizophrenia and relationships with symptoms. *Psychological medicine*, 48(15):2492–2499.
- Fornito, A., Zalesky, A., and Bullmore, E. (2016). *Fundamentals of brain network analysis*. Academic Press.
- Gao, C., Ma, Z., Zhang, A. Y., and Zhou, H. H. (2017). Achieving optimal misclassification proportion in stochastic block models. *The Journal of Machine Learning Research*, 18(1):1980–2024.
- Gaznick, N., Tranel, D., McNutt, A., and Bechara, A. (2014). Basal ganglia plus insula damage yields stronger disruption of smoking addiction than basal ganglia damage alone. *nicotine & tobacco research*, 16(4):445–453.
- Govaert, G. and Nadif, M. (2008). Block clustering with bernoulli mixture models: Comparison of different approaches. *Computational Statistics & Data Analysis*, 52(6):3233–3245.

- Grünwald, P. D. (2007). *The minimum description length principle*. MIT press.
- Hartigan, J. A. (1972). Direct clustering of a data matrix. *Journal of the american statistical association*, 67(337):123–129.
- J. K. Gupta, S. Singh, N. K. V. (2013). Mtba: Matlab toolbox for biclustering analysis. pages 94–97. IEEE.
- Jiang, X., Zhang, T., Zhang, S., Kendrick, K. M., and Liu, T. (2021). Fundamental functional differences between gyri and sulci: implications for brain function, cognition, and behavior. *Psychoradiology*, 1(1):23–41.
- Kamvar, S., Klein, D., and Manning, C. (2003). Spectral learning. Technical Report 2003-25, Stanford InfoLab.
- Li, R., Zhong, W., and Zhu, L. (2012a). Feature screening via distance correlation learning. *Journal of the American Statistical Association.*, 107(499):1129–1139.
- Li, R., Zhong, W., and Zhu, L. (2012b). Feature screening via distance correlation learning. *Journal of the American Statistical Association*, 107(499):1129–1139.
- Loewe, K., Grueschow, M., Stoppel, C. M., Kruse, R., and Borgelt, C. (2014). Fast construction of voxel-level functional connectivity graphs. *BMC neuroscience*, 15(1):1–13.
- Luxburg, U., Bousquet, O., and Belkin, M. (2004). Limits of spectral clustering. *Advances in neural information processing systems*, 17.
- Lynall, M.-E., Bassett, D. S., Kerwin, R., McKenna, P. J., Kitzbichler, M., Muller, U., and Bullmore, E. (2010). Functional connectivity and brain networks in schizophrenia. *Journal of Neuroscience*, 30(28):9477–9487.
- McClernon, F. J., Conklin, C. A., Kozink, R. V., Adcock, R. A., Sweitzer, M. M., Addicott, M. A., Chou, Y.-h., Chen, N.-k., Hallyburton, M. B., and DeVito, A. M. (2016). Hippocampal and insular response to smoking-related environments: neuroimaging evidence for drug-context effects in nicotine dependence. *Neuropsychopharmacology*, 41(3):877–885.
- Moran, L. V., Sampath, H., Kochunov, P., and Hong, L. E. (2013). Brain circuits that link schizophrenia to high risk of cigarette smoking. *Schizophrenia bulletin*, 39(6):1373–1381.
- Nichols, T. E. (2012). Multiple testing corrections, nonparametric methods, and random field theory. *Neuroimage*, 62(2):811–815.
- Nichols, T. E. and Holmes, A. P. (2002). Nonparametric permutation tests for functional neuroimaging: a primer with examples. *Human brain mapping*, 15(1):1–25.

- Palaniyappan, L., White, T. P., and Liddle, P. F. (2012). The concept of salience network dysfunction in schizophrenia: from neuroimaging observations to therapeutic opportunities. *Current topics in medicinal chemistry*, 12(21):2324–2338.
- Rubinov, M. and Sporns, O. (2010). Complex network measures of brain connectivity: uses and interpretations. *Neuroimage*, 52(3):1059–1069.
- Shi, J. and Malik, J. (2000). Normalized cuts and image segmentation. *IEEE Transactions on pattern analysis and machine intelligence*, 22(8):888–905.
- Simpson, S. L., Bowman, F. D., and Laurienti, P. J. (2013). Analyzing complex functional brain networks: Fusing statistics and network science to understand the brain. *Statistics Surveys*, 7:1–36.
- St. Jacques, P. L., Dolcos, F., and Cabeza, R. (2009). Effects of aging on functional connectivity of the amygdala for subsequent memory of negative pictures: a network analysis of functional magnetic resonance imaging data. *Psychological science*, 20(1):74–84.
- Sutherland, M. T. and Stein, E. A. (2018). Functional neurocircuits and neuroimaging biomarkers of tobacco use disorder. *Trends in molecular medicine*, 24(2):129–143.
- Thirion, B., Flandin, G., Pinel, P., Roche, A., Ciuciu, P., and Poline, J.-B. (2006). Dealing with the shortcomings of spatial normalization: Multi-subject parcellation of fmri datasets. *Human brain mapping*, 27(8):678–693.
- Wetherill, R. R., Jagannathan, K., Shin, J., and Franklin, T. R. (2014). Sex differences in resting state neural networks of nicotine-dependent cigarette smokers. *Addictive behaviors*, 39(4):789–792.
- Wig, G. S., Laumann, T. O., and Petersen, S. E. (2014). An approach for parcellating human cortical areas using resting-state correlations. *Neuroimage*, 93:276–291.
- Woo, C.-W., Krishnan, A., and Wager, T. D. (2014). Cluster-extent based thresholding in fmri analyses: pitfalls and recommendations. *Neuroimage*, 91:412–419.
- Wu, G.-R., Stramaglia, S., Chen, H., Liao, W., and Marinazzo, D. (2013). Mapping the voxel-wise effective connectome in resting state fmri. *PloS one*, 8(9):e73670.
- Wu, Q., Huang, X., Culbreth, A. J., Waltz, J. A., Hong, L. E., and Chen, S. (2021a). Extracting brain disease-related connectome subgraphs by adaptive dense subgraph discovery. *Biometrics*.
- Wu, Q., Zhang, Y., Huang, X., Ma, T., Hong, L. E., Kochunov, P., and Chen, S. (2021b). A multivariate to multivariate approach for voxel-wise genome-wide association analysis. *bioRxiv*.

- Wylie, K. P. and Tregellas, J. R. (2010). The role of the insula in schizophrenia. *Schizophrenia research*, 123(2-3):93–104.
- Xia, Y. and Li, L. (2017). Hypothesis testing of matrix graph model with application to brain connectivity analysis. *Biometrics*, 73(3):780–791.
- Xia, Y. and Li, L. (2019). Matrix graph hypothesis testing and application in brain connectivity alternation detection. *Statistica Sinica*, 29(1):303–328.
- Zalesky, A., Fornito, A., and Bullmore, E. T. (2010). Network-based statistic: identifying differences in brain networks. *Neuroimage*, 53(4):1197–1207.